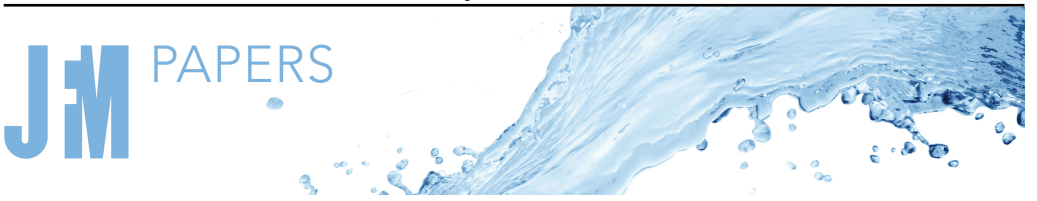
J. Fluid Mech. (2026), *vol.* 1037, A22, doi:10.1017/jfm.2026.11688



Dispersive effects on equatorial shallow-water shock waves

Chen Wang[1,2], **Dong Shao**[3] **and Zhan Wang**[3,4]

[1]Research Center of Mathematics, Advanced Institute of Natural Sciences, Beijing Normal University, Zhuhai 519087, PR China

[2]Department of Mathematical Sciences, Beijing Normal–Hong Kong Baptist University, Zhuhai 519087, PR China

[3]Key Laboratory for Mechanics in Fluid Solid Coupling Systems, Institute of Mechanics, Chinese Academy of Sciences, Beijing 100190, PR China

[4]State Key Laboratory of High Temperature Gas Dynamics, Institute of Mechanics, Chinese Academy of Sciences, Beijing 100190, PR China

Corresponding author: Zhan Wang, zwang@imech.ac.cn

(Received 1 October 2025 UTC; revised 14 May 2026 UTC; accepted 14 May 2026 UTC)

The nonlinear dynamics of equatorial shallow-water waves is examined both theoretically and numerically. While unidirectional Kelvin waves are non-dispersive and can evolve into shocks, they also excite Poincaré waves which are dispersive. This dispersion significantly impacts the dynamics of the shock. A reduced model has been developed to describe the behaviours of the Kelvin wave and the first Poincaré wave, where the dispersive term appears in a form similar to that in the Ostrovsky equation. The findings indicate that a sharp spike forms in the profile of the first Poincaré wave, resulting in an overshoot of the shock. Theoretical predictions are validated through numerical simulations of the primitive equations.

Key words: shallow water flows, waves in rotating fluids

1. Introduction

Shallow-water models are widely utilised in both geophysical and astrophysical fluid dynamics. By assuming much larger horizontal length scales than the vertical scale, these models effectively capture the essential dynamics of large-scale motions in the ocean, atmosphere and astrophysical flows. This paper focuses on the equatorial shallow-water system on a β-plane, where the Coriolis force varies linearly with latitude. Near the equator, the rotation serves as a waveguide, confining waves to the equatorial region. These waves are known as equatorial shallow-water waves.

© The Author(s), 2026. Published by Cambridge University Press.

https://doi.org/10.1017/jfm.2026.11688 Published online by Cambridge University Press

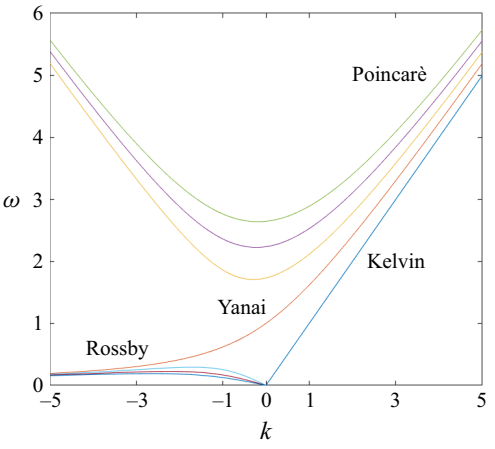


Figure 1. Dispersion relations of linear equatorial shallow-water waves. The wavenumber k and frequency ω have been rescaled by $\beta^{1/2}(gH)^{-1/4}$ and $\beta^{1/2}(gH)^{1/4}$, respectively, where β represents the gradient of the Coriolis parameter, g is the acceleration due to gravity and H denotes the mean depth of the fluid layer.

The linear dynamics of equatorial shallow-water waves was first studied by Matsuno (1966), who derived dispersion relations for various wave types. Using terminology introduced later (e.g. Majda *et al.* 1999; Pedlosky 2013), these waves are classified as Kelvin, Poincaré, Rossby and Yanai waves. Their dispersion relations are illustrated in figure 1. Kelvin waves have a constant phase velocity that is independent of wavelength and propagate eastward. Poincaré waves, also known as inertio-gravity waves, exhibit high phase velocities and can propagate both eastward and westward. Rossby waves, which are influenced by the β-effect, propagate westward. These waves are analogous to those in more familiar contexts, such as shallow water on an f-plane or two-dimensional flow on a β-plane. Yanai waves, also referred to as mixed Rossby–gravity waves, have dispersion curves that connect Rossby waves and eastward-propagating Poincaré waves. Matsuno's theory has been validated by numerous observations in both the ocean and the atmosphere (e.g. Yanai & Maruyama 1966; Wallace & Kousky 1968; see Kiladis *et al.* 2009 for a review).

Equatorial shallow-water waves play a crucial role in significant climate phenomena such as El Niño and the Madden–Julian Oscillation (MJO). During El Niño, the temperature initially increases in the western Pacific. Eastward-propagating Kelvin waves then transport this heat to the eastern Pacific, leading to a temperature rise (Straub, Kiladis & Ciesielski 2006; Fedorov & Brown 2009). The MJO refers to variations in tropical precipitation, driven by a coherent structure of varying moisture that moves eastward through the atmosphere. A recent theory suggests that these coherent structures can be understood as 'modons', which are pairs of moving vortices in equatorial shallow water. The dynamics of modons are closely related to nonlinear Rossby waves (Yano & Tribia 2017; Rostami & Zeitlin 2019*a*,*b*). Recent studies have demonstrated that more realistic shallow-water models, which incorporate moisture convection, can predict modons that capture essential features of the MJO (Rostami & Zeitlin 2020; Rostami, Zhao & Petri 2022; Cao *et al.* 2025).

A notable characteristic of the shallow-water model is the tendency to form shocks. A shock is a discontinuity in either velocity or surface height and is significant in geophysics. In oceanic contexts, a shock may signal wave overturning or indicate hydraulic jumps, both of which can lead to wave breaking (Fedorov & Melville 1995, 2000). The

https://doi.org/10.1017/jfm.2026.11688 Published online by Cambridge University Press

mechanism behind shock formation is now well understood. The shallow-water equations, when rotation is not considered, are equivalent to those governing compressible gases, which are known for their ability to produce shocks (Whitham 1974; Lighthill 1978). When rotation is included – either in coastal shallow water on an f-plane (Bennett 1973; Fedorov & Melville 1995) or in equatorial shallow water on a β-plane (Boyd 1980; Ripa 1982) – Kelvin waves can develop into shocks. The non-dispersive nature of Kelvin waves is crucial in this nonlinear evolution, as there is no dispersive mechanism for energy radiation. Meanwhile, nonlinear advection terms dominate as wave amplitudes increase, causing wavefronts to steepen. Additionally, studies show that shock formation can be effectively approximated using the Burgers equation (Burgers 1948).

Numerical simulations of the evolution of Kelvin waves in the equatorial shallow-water system have been conducted by Fedorov & Melville (2000), Le Sommer, Reznik & Zeitlin (2004) and Bouchut, Le Sommer & Zeitlin (2005). Their findings confirm that Kelvin waves evolve into shocks, showing qualitative agreements with the theories proposed by Boyd (1980) and Ripa (1982). However, the simulation results indicate that the shocks exhibit complex profiles with very small-scale structures, which are not captured by the simple jump predicted by the Burgers equation. Fedorov & Melville (2000) provided an insightful explanation for this phenomenon. They revealed that the complex shock profile arises from the first Poincaré wave excited by the Kelvin wave. Additionally, they proposed a mechanism for this excitation: nonlinearity causes the Kelvin wave to travel faster, allowing it to catch up with the Poincaré wave and achieve resonance.

In this paper, we conduct a theoretical study of the dynamic behaviours of equatorial shallow-water waves, focusing particularly on the role of Poincaré waves. While Fedorov & Melville (2000) primarily explored these waves through direct numerical simulations, our objective is to develop a reduced model that enhances our understanding of the nonlinear dynamics of both the Kelvin wave and the first Poincaré wave, offering deeper physical insights. Our analysis demonstrates that the velocity of the Kelvin wave does not need to precisely match that of the Poincaré wave for the latter to be generated. Notably, excitation can occur even with a slight difference in their phase velocities. Additionally, our model is computationally efficient, enabling ultrahigh resolutions that allow us to uncover the detailed structure of shocks.

A central topic of this study is the effects of dispersion introduced by Poincaré waves. The impact of dispersion in linear waves is well understood; however, its effects in nonlinear waves are significantly more complex, especially concerning shocks. In the Korteweg–de Vries (KdV) and nonlinear Schrödinger (NLS) equations, it has been shown that dispersion smooths the discontinuities of shock waves and results in high-frequency quasi-periodic oscillations (see e.g. El & Hoefer 2016; Carretero-Gonzalez, Frantzeskakis & Kevrekidis 2024). In geophysical fluid dynamics, nonlinear one-dimensional Poincaré waves can be modelled using the Ostrovsky equation (Ostrovsky 1978). A further simplified version of the Ostrovsky equation, which considers rotation as the sole source of dispersion, is known as the reduced Ostrovsky equation or the Hunter–Ostrovsky equation. Research has shown that while the dispersion weakens the shocks, waves with sufficiently large amplitudes or short wavelengths can still produce shocks (Hunter 1990; Boyd 2005*a*; Grimshaw, Helfrich & Johnson 2012).

In the absence of dispersion, Wang, Wang & Hajduk (2020) investigated the nonlinear interaction between the Kelvin wave and the first Poincaré wave. They examined a scenario involving significantly short waves, where the phase velocities of both waves are identical. Their theory predicts that the Poincaré wave exhibits a simple jump at the shock, similar to that of the Kelvin wave. However, results from direct numerical simulations reveal more complex shock structures, which they suggest may arise from dispersion.

https://doi.org/10.1017/jfm.2026.11688 Published online by Cambridge University Press

The remainder of the paper is organised as follows. In § 2, we present the governing equations for the equatorial shallow-water system. In § 3, we conduct a theoretical analysis to derive a reduced model for the dynamics of the Kelvin wave and the first Poincaré wave. We summarise the model in § 4, solve it numerically and use the solutions to investigate the dynamics of dispersive shocks. In § 5, we perform numerical simulations on the equatorial shallow-water equations and compare the results with our theoretical predictions. Finally, we draw our conclusions in § 6.

2. Governing equations

The mechanism and properties of equatorial waves can be illustrated by considering horizontally propagating waves in a rotating fluid of uniform finite depth H, where H is small compared with the horizontal extent of the fluid. The fluid is assumed to have a homogeneous density and a free surface. This idealised representation is referred to in geophysical fluid dynamics as a shallow-water model. Specifically, we consider equatorial shallow-water flow on a β-plane, where the Coriolis parameter is $f = \beta y$, with y denoting latitude and x denoting longitude. Let the velocities in the (x, y) directions be represented as (u, v), and the surface deformation as η; then, the governing equations of the system read

$$u_t + uu_x + vu_y - \beta yv = -g\eta_x, \tag{2.1a}$$
$$v_t + uv_x + vv_y + \beta yu = -g\eta_y, \tag{2.1b}$$
$$\eta_t + [u(H+\eta)]_x + [v(H+\eta)]_y = 0, \tag{2.1c}$$

where the subscripts denote partial differentiation. By using

$$L = \beta^{-1/2}(gH)^{1/4}, \quad T = \beta^{-1/2}(gH)^{-1/4}, \quad \frac{L}{T}, \quad H \tag{2.2}$$

to rescale (x, y), t, (u, v) and η, we can derive the corresponding non-dimensional equations:

$$u_t + uu_x + vu_y - yv = -\eta_x, \tag{2.3a}$$
$$v_t + uv_x + vv_y + yu = -\eta_y, \tag{2.3b}$$
$$\eta_t + [u(1+\eta)]_x + [v(1+\eta)]_y = 0. \tag{2.3c}$$

We consider periodic boundary conditions in the x direction, while $(u, v, \eta) \to 0$ as $y \to \pm\infty$. The equations in system (2.3) are the primitive dimensionless equations for equatorial shallow-water waves. In § 3, we perform a theoretical analysis of these equations and derive a reduced model for the nonlinear dynamics of the Kelvin wave and the first Poincaré wave. Readers who prefer not to delve into details of the mathematical derivation can skip ahead to § 4.1, where we summarise the model. Additionally, we numerically solve system (2.3) in § 5 to validate our theoretical findings.

3. A theoretical analysis

In this section, we conduct a theoretical analysis of equatorial shallow-water waves. Our analytical progress involves asymptotic analysis at small amplitudes and short wavelengths. In § 3.1, we undertake a linear analysis, from which we demonstrate potential resonance between waves. Then, in § 3.2, we derive the evolution equations for the nonlinear waves.

https://doi.org/10.1017/jfm.2026.11688 Published online by Cambridge University Press

3.1. *Linear analysis*

Linear shallow-water equatorial waves have been studied by Matsuno (1966), who has given the complete spectrum. Here, the focus is on short Yanai and Poincaré waves with phase velocities close to those of Kelvin waves. In particular, we derive a linear wave equation with a dispersive term, providing a foundation to build the nonlinear wave equations.

To study the linear waves, we omit the product terms in (2.3) considering small wave amplitudes, and obtain the linearised equations:

$$u_t - yv + \eta_x = 0, \quad v_t + yu + \eta_y = 0, \quad \eta_t + u_x + v_y = 0. \tag{3.1}$$

To address the y dependence, a common approach is to assume normal modes in both x and t, such as $u = \hat{u}(y)\mathrm{e}^{\mathrm{i}(kx-\omega t)}$, and then solve the ordinary differential equations in y to derive the dispersion relation. However, in the present problem, our main objective is to derive simplified wave equations, so we take a different approach: we retain the dependence on x and t while expanding the variables in terms of their eigenfunctions in y. Boyd (1980) introduced an effective technique for this approach, which we will adopt.

Boyd (1980) suggested that the derivation can be significantly simplified by considering the sum and difference of η and u:

$$S = \eta + u, \qquad D = \eta - u. \tag{3.2}$$

The equations for S and D are given by

$$S_t + S_x + \left(\frac{\partial}{\partial y} - y\right) v = 0, \tag{3.3a}$$

$$v_t + \frac{1}{2}\left(\frac{\partial}{\partial y} + y\right) S + \frac{1}{2}\left(\frac{\partial}{\partial y} - y\right) D = 0, \tag{3.3b}$$

$$D_t - D_x + \left(\frac{\partial}{\partial y} + y\right) v_x = 0. \tag{3.3c}$$

Both S and D can be expressed in terms of their eigenfunctions in y, based on the linear theory proposed by Matsuno (1966):

$$(S,\, v,\, D) = \mathrm{e}^{-y^2/2} \sum_{n=0}^{\infty} [S_n(x,t),\, v_n(x,t),\, D_n(x,t)]\, \frac{H_n(y)}{2^n}, \tag{3.4}$$

where H_n represents the nth-order Hermite polynomial. For convenience, we list the first five Hermite polynomials:

$$\begin{aligned} &H_0 = 1, \qquad H_1 = 2y, \qquad H_2 = 4y^2 - 2, \\ &H_3 = 8y^3 - 12y, \qquad H_4 = 16y^4 - 48y^2 + 12. \end{aligned} \tag{3.5}$$

Boyd (1980) noted that the differential operators in (3.3) correspond to those found in the recurrence relations of the eigenfunctions:

$$\left(\frac{\partial}{\partial y} - y\right)\left[H_n(y)\mathrm{e}^{-y^2/2}\right] = -H_{n+1}(y)\mathrm{e}^{-y^2/2}, \tag{3.6a}$$

$$\left(\frac{\partial}{\partial y} + y\right)\left[H_n(y)\mathrm{e}^{-y^2/2}\right] = 2nH_{n-1}(y)\mathrm{e}^{-y^2/2}. \tag{3.6b}$$

https://doi.org/10.1017/jfm.2026.11688 Published online by Cambridge University Press

This relation enables us to easily derive the equations for each order of expression (3.4). Specifically, for $n = 0$, we have

$$S_{0,t} + S_{0,x} = 0\,; \tag{3.7}$$

for $n = 1$,

$$S_{1,t} + S_{1,x} - v_0 = 0, \quad v_{0,t} + S_1 = 0\,; \tag{3.8}$$

and for $n \geq 2$,

$$S_{n,t} + S_{n,x} - v_{n-1} = 0, \tag{3.9a}$$

$$v_{n-1,t} + nS_n - \frac{1}{2}D_{n-2} = 0, \tag{3.9b}$$

$$D_{n-2,t} - D_{n-2,x} + 2(n-1)v_{n-1} = 0. \tag{3.9c}$$

Equations (3.7) and (3.8) describe the dynamics of Kelvin waves and Yanai waves, respectively, and system (3.9) incorporates Rossby waves and Poincaré waves. By applying the normal mode form proportional to $\mathrm{e}^{\mathrm{i}(kx-\omega t)}$, the non-trivial conditions from (3.7)–(3.9) yield the dispersion relations. For $n = 0$, (3.7) gives the frequency of the Kelvin wave:

$$\omega = k. \tag{3.10}$$

For $n = 1$, system (3.8) gives the dispersion relation for the Yanai wave:

$$\omega - k - \frac{1}{\omega} = 0. \tag{3.11}$$

For $n \geq 2$, system (3.9) results in the dispersion relation for Poincaré and Rossby waves:

$$\omega^2 - k^2 - \frac{k}{\omega} = 2n - 1. \tag{3.12}$$

Numerical solutions of these dispersion relations are plotted in figure 1. Various types of resonance are possible among linear equatorial shallow-water waves, leading to nonlinear interactions among different modes. For a comprehensive overview of triad interactions and resonance involving wave packets, the interested reader is referred to Ripa (1983*a*,*b*) and Boyd (1983). In the present study, we concentrate on the resonance of Kelvin waves within a continuous spectrum. The Kelvin wave is non-dispersive, meaning its phase velocity ($\omega/k = 1$) is constant. As a result, waves of differing wavelengths can resonate and produce nonlinear evolution (Boyd 1980; Ripa 1982).

Short Yanai and Poincaré waves may resonate with Kelvin waves due to their similar phase velocities. Their dispersion relations (3.11) and (3.12) indicate that as $k \to \infty$, one of the limits of ω/k is unity, which corresponds to the phase velocity of the Kelvin wave. The interaction of these three types of waves in this limit has been investigated by Wang *et al.* (2020). In the current study, we focus on the scenario where k is large but finite. For instance, figure 1 shows that at approximately $k = 5$, the phase velocities of the Yanai and Poincaré waves differ only slightly from those of the Kelvin wave. We therefore examine the large-k behaviour of (3.8) and (3.9). Assuming that the waves are characterised by $\mathrm{e}^{\mathrm{i}k(x-ct)}$, where k is large and c is close to unity, (3.9*c*) indicates that, at leading order,

$$D_{n-2,t} - D_{n-2,x} = 2D_{n-2,t} = -2(n-1)\,v_{n-1}. \tag{3.13}$$

It then follows that

$$D_{n-2} = -(n-1)\int v_{n-1}\,\mathrm{d}t = v_{n-1} \times O\left(k^{-1}\right), \tag{3.14}$$

https://doi.org/10.1017/jfm.2026.11688 Published online by Cambridge University Press

suggesting that D_{n-2} is much smaller than v_{n-1}. Next, we consider (3.9*b*). By comparing the orders of $v_{n-1,t}$ and D_{n-2}, one can demonstrate using (3.14) that

$$v_{n-1,t} = v_{n-1} \times O(k), \qquad -\frac{1}{2} D_{n-2} = v_{n-1} \times O\left(k^{-1}\right). \tag{3.15}$$

This suggests that, in the limit of large k, $v_{n-1,t}$ is significantly larger than D_{n-2} in (3.9*b*). Therefore, we can neglect the latter and derive

$$v_{n-1} = -n \int S_n \, \mathrm{d}t. \tag{3.16}$$

Equation (3.16) shows that S_n is of the order of k larger than v_{n-1}, making it $O(k^2)$ larger than D_{n-2} according to (3.14). Consequently, we can disregard the difference between η and u for large wavenumbers. If we define η_n and u_n similarly to (3.4), we find that

$$u_n = \eta_n = \frac{S_n}{2} \equiv A_n. \tag{3.17}$$

Substituting (3.16) and (3.17) into (3.9*a*) results in the evolution equation:

$$A_{n,t} + A_{n,x} + n \int A_n \, \mathrm{d}t = 0. \tag{3.18}$$

We can verify that this holds for $n = 0$ and $n = 1$ in (3.7) and (3.8) as well.

Equation (3.18) describes the linear evolution of Kelvin, Yanai and Poincaré waves at large wavenumbers. The leading order of this equation is $A_{n,t} + A_{n,x} = 0$, which represents non-dispersive transport, and the integral term accounts for dispersion at the next order. This is more clearly illustrated by examining the dispersion relation of (3.18):

$$\omega - k - \frac{n}{\omega} = 0, \tag{3.19}$$

where the term $-n/\omega$ indicates weak dispersion at large wavenumber k. Additionally, it can be verified that (3.19) is consistent with (3.10) and (3.11), and it represents the large-k limit of (3.12). To illustrate the role of dispersion in wave modulation, we can examine the dependence on the variables

$$\theta = k(x - t) \quad \text{and} \quad \tau = \delta t, \tag{3.20}$$

where θ represents the phase of the non-dispersive part of the wave and τ, with $\delta \ll 1$, reflects slow wave modulation. The leading-order modulation equation is then given by

$$A_{n,\tau} - \frac{n}{k\delta} \int A_n \, \mathrm{d}\theta = 0, \tag{3.21}$$

which shows that modulation is driven by the integral dispersive term. Note that the integral term is no longer small if $\delta = O(k^{-1})$, but we will specify δ through nonlinear analysis, where nonlinearity decides the time scale of wave modulation. Additionally, it is worth noting that (3.21) consists of $O(\delta)$ terms of (3.18), suggesting that even weak nonlinearity can contribute to modulation, which we explore next.

3.2. *The nonlinear analysis*

Having identified the potential resonance between linear waves, we set out to investigate the resulting nonlinear dynamics. We limit our attention to the nonlinear evolution of an initially linear Kelvin wave, which is responsible for shock formation, and leave the study of other initial conditions for future research. At an early stage, the wave field is given by

$$u = \eta = \varepsilon \mathrm{e}^{-y^2/2} \sin(kx - kt), \quad v = 0, \quad \text{for} \quad t \ll 1, \tag{3.22}$$

https://doi.org/10.1017/jfm.2026.11688 Published online by Cambridge University Press

where ε is a small parameter representing the order of the wave amplitude. In our linear analysis, we demonstrated that short Poincaré waves have phase velocities close to that of the Kelvin wave and can therefore be excited by the latter. We restrict our nonlinear analysis to the dynamics of the Kelvin wave and the first Poincaré wave. The Yanai wave is excluded on the grounds of symmetry: since both the initial Kelvin wave and the newly excited Poincaré waves are even in y, they have zero projection onto the odd eigenspace of the Yanai wave. Furthermore, previous numerical simulations (Fedorov & Melville 2000) suggest that the first Poincaré wave dominates the response during Kelvin wave evolution, while higher-order modes remain negligible. This is consistent with our analysis, which indicates that the initial Kelvin wave exerts only weak forcing on these higher-order modes. Consequently, we neglect higher-order Poincaré waves and assume that the dynamics is primarily governed by the first mode. We acknowledge that we do not have a rigorous justification for this assumption; its validity will be assessed *a posteriori* through comparison with numerical simulations.

There are two scenarios for this excitation of the first Poincaré wave. The first scenario begins with a short Kelvin wave, meaning that the wavenumber k is large. This wave then excites short Poincaré waves through a resonance mechanism. The second scenario starts with a long linear Kelvin wave, which cannot directly excite Poincaré waves. However, this Kelvin wave evolves into a shock that has a small length scale, where the Poincaré waves are excited locally. In the following, we analyse the first scenario and derive a reduced model for the nonlinear wave dynamics. We have found that the same reduced model is also applicable to the second scenario, which we briefly discuss at the end of this section.

We again adopt the variables S and D as defined in (3.2), but now retain the nonlinear terms in the primitive (2.3). These equations may be rearranged to yield

$$S_t + S_x + \left(\frac{\partial}{\partial y} - y\right) v = -uu_x - (u\eta)_x - vu_y - (v\eta)_y \equiv F, \tag{3.23a}$$

$$v_t + \frac{1}{2}\left(\frac{\partial}{\partial y} + y\right) S + \frac{1}{2}\left(\frac{\partial}{\partial y} - y\right) D = -uv_x - vv_y \equiv E, \tag{3.23b}$$

$$D_t - D_x + \left(\frac{\partial}{\partial y} + y\right) v_x = uu_x - (u\eta)_x + vu_y - (v\eta)_y \equiv G. \tag{3.23c}$$

The nonlinear terms are defined as F, E and G, and we expand them by the eigenfunctions of linear waves as in (3.4):

$$(F, E, G) = \mathrm{e}^{-y^2/2} \sum_{n=0}^{\infty} [F_n(x,t), E_n(x,t), G_n(x,t)] \frac{H_n(y)}{2^n}. \tag{3.24}$$

The projection onto each eigenfunction is calculated by exploiting the completeness and orthogonality of the Hermite polynomials; for instance, the coefficients are given by

$$F_n = \frac{\displaystyle\int_{-\infty}^{\infty} F H_n(y) \mathrm{e}^{-y^2/2}\, \mathrm{d}y}{\sqrt{\pi} n!}, \tag{3.25}$$

with analogous expressions for E_n and G_n. Substituting (3.4) and (3.24) into (3.23) and isolating the $n = 0$ and $n = 2$ components, which correspond to the Kelvin wave and the first Poincaré wave, respectively, we arrive at the governing equations. Given that the linear terms are identical to those in (3.7) and (3.9), this procedure yields

$$S_{0,t} + S_{0,x} = F_0 \tag{3.26}$$

https://doi.org/10.1017/jfm.2026.11688 Published online by Cambridge University Press

and

$$S_{2,t} + S_{2,x} - v_1 = F_2, \tag{3.27a}$$

$$v_{1,t} + 2S_2 - \frac{1}{2}D_0 = E_1, \tag{3.27b}$$

$$D_{0,t} - D_{0,x} + 2v_1 = G_0. \tag{3.27c}$$

The initial condition derived from (3.22) is given by

$$S_0 = 2\varepsilon \sin(kx - kt), \quad S_2 = v_1 = D_0 = 0, \quad t \to 0, \tag{3.28}$$

signifying a pure Kelvin wave state with no Poincaré wave component. Under the condition of a large wavenumber k, the phase velocity of the first Poincaré wave nearly matches that of the Kelvin wave, facilitating a resonant-like excitation. Consequently, the first Poincaré wave eventually attains an amplitude comparable to that of the Kelvin wave, such that

$$S_0, \ S_2 = O(\varepsilon). \tag{3.29}$$

We proceed with our analysis based on this scaling. The detailed mechanism by which S_2 grows to $O(\varepsilon)$, involving the evolution of incipient Poincaré waves driven by a linear Kelvin wave with a close phase velocity, is provided in Appendix A.

We further simplify the model by exploiting the asymptotic limit of large k. Based on the properties of linear and weakly nonlinear waves given in (3.13), (3.16), (3.29) and (A9), the variables u, v and η scale as

$$u, \eta = O(\varepsilon), \quad v = O\left(\varepsilon k^{-1}\right). \tag{3.30}$$

From (3.23) and (3.25), we can subsequently estimate the orders of the nonlinear terms as

$$F_0, \ F_2 = O\left(k\varepsilon^2\right), \quad E_1 = O\left(\varepsilon^2\right), \quad G_0 = O\left(k\varepsilon^2\right). \tag{3.31a,b,c}$$

Introducing the phase variables defined in (3.20), we can show that the terms in (3.27*b*,*c*) scale as

$$v_{1,t} \simeq -kv_{1,\theta} = O(k\varepsilon) \gg E_1, \quad D_{0,t} - D_{0,x} \simeq -2kD_{0,\theta} = O(k\varepsilon) \gg G_0. \tag{3.32}$$

Consequently, the nonlinear terms E_1 and G_0 drop off the leading order, ensuring that the linear relations (3.13)–(3.17) remain valid:

$$v_1 = -2\int S_2 \, \mathrm{d}t \quad \text{and} \quad u_n = \eta_n = \frac{S_n}{2} \equiv A_n, \quad \text{for } n = 0, 2, \tag{3.33}$$

and $D_0 = O(k^{-2}) \times S_2$ is of a higher order. Substitution (3.33) into (3.27*a*) yields

$$A_{n,t} + A_{n,x} + n\int A_n \, \mathrm{d}t = \frac{1}{2}F_n, \quad \text{for } n = 0, 2. \tag{3.34}$$

For the first Poincaré wave ($n = 2$), and invoking (3.20) and (3.31*a*), the advection, dispersion and nonlinear terms scale, respectively, as

$$A_{2,t} + A_{2,x} = O(\delta\varepsilon), \quad 2\int A_2 \, \mathrm{d}t = O\left(k^{-1}\varepsilon\right), \quad \frac{1}{2}F_2 = O\left(k\varepsilon^2\right). \tag{3.35}$$

Notably, the leading-order contributions to $A_{2,t}$ and $A_{2,x}$ cancel via their dependence on the fast phase θ. This cancellation results in a slow modulation where weak dispersion and nonlinearity enter the dominant balance. Requiring these three terms to be of the same order in (3.35) yields the characteristic scales

$$\delta \sim k\varepsilon, \quad k \sim \varepsilon^{-1/2}, \tag{3.36a,b}$$

https://doi.org/10.1017/jfm.2026.11688 Published online by Cambridge University Press

which define the temporal and spatial scales of the modulation. To evaluate F_n in (3.34) explicitly, we express u and η by superimposing the Kelvin and first Poincaré waves at large k:

$$u = \eta = \mathrm{e}^{-y^2/2}\left[A_0(x,t) + \left(y^2 - \frac{1}{2}\right)A_2(x,t)\right]. \tag{3.37}$$

Substitution of the above expressions into (3.23*a*) yields

$$F \simeq -uu_x - (u\eta)_x = -\frac{3}{2}\mathrm{e}^{-y^2}\left[A_0^2 + \left(y^2 - \frac{1}{2}\right)^2 A_2^2 + (2y^2 - 1)A_0A_2\right]_x. \tag{3.38}$$

Performing the projection (3.25), we find

$$\begin{aligned} F_0 &= \sqrt{\frac{2}{3}}\left[-\frac{3}{2}A_0^2 - \frac{3}{8}A_2^2 + \frac{1}{2}A_0A_2\right]_x, \\ F_2 &= \sqrt{\frac{2}{3}}\left[\frac{1}{2}A_0^2 - \frac{13}{24}A_2^2 - \frac{3}{2}A_0A_2\right]_x. \end{aligned} \tag{3.39}$$

We also find $F_1 = 0$ since F is an even function of y whereas $H_1(y) = 2y$ is odd; this confirms that the Yanai wave is not excited, consistent with our earlier symmetry arguments. Substitution of (3.39) into (3.34) ultimately provides the evolution equations for A_0 and A_2:

$$A_{0,t} + A_{0,x} = \sqrt{\frac{2}{3}}\left[-\frac{3}{4}A_0^2 - \frac{3}{16}A_2^2 + \frac{1}{4}A_0A_2\right]_x, \tag{3.40a}$$

$$A_{2,t} + A_{2,x} + 2\int A_2\,\mathrm{d}t = \sqrt{\frac{2}{3}}\left[\frac{1}{4}A_0^2 - \frac{13}{48}A_2^2 - \frac{3}{4}A_0A_2\right]_x. \tag{3.40b}$$

For the integral term, we require that its result only contains wave components without adding additional constants, consistent with our treatment of (3.18). This requirement is more conveniently described in terms of wave phase later in § 4.1. The initial condition is

$$A_0 = \varepsilon\sin(kx - kt), \quad A_2 = 0, \quad \text{as } t \to 0, \tag{3.41}$$

which specifies a linear Kelvin wave at early times in accordance with (3.22). We apply spatial periodic boundary conditions to (3.40) consistent with (3.41). Thus, we have derived a reduced model for the nonlinear dynamics of the Kelvin wave and the first Poincaré wave when the wavenumber is large. Notably, the integral term in (3.40*b*) represents the effect of dispersion.

Next, we comment on the second scenario where k is not large. In this case, the first Poincaré wave is not excited by a linear Kelvin wave, and instead, the Kelvin wave resonates with itself, leading to nonlinear evolution governed by the equation

$$A_{0,t} + A_{0,x} = \sqrt{\frac{3}{8}}\left(A_0^2\right)_x. \tag{3.42}$$

This is an inviscid Burgers equation, which exhibits shock formation over time. The shock has a very small length scale and travels at a velocity of unity (see § 4.2 and figure 3 appearing later), which is the phase velocity of the Poincaré wave as $k \to \infty$; thus the condition to excite the Poincaré waves is satisfied locally at the shock. To furnish a local asymptotic analysis, we can adopt a scaling analogous to (3.20):

$$\theta = \kappa(x - t), \quad \tau = \delta t, \tag{3.43}$$

https://doi.org/10.1017/jfm.2026.11688 Published online by Cambridge University Press

where $\kappa \gg 1$ signifies the small length scale of the shock. In the large-κ limit, the scaling relations (3.30)–(3.36) remain valid with k replaced by κ, leading again to the shock dynamics described by (3.40). On the other hand, the length scale is no longer small away from the shock region. There, the Poincaré wave driven by the Kelvin wave is still governed by (3.20), but k is not large. Consequently, the terms in (3.34) scale as

$$A_{2,t} + A_{2,x} \ll 2 \int A_2 \, \mathrm{d}t \sim \frac{1}{2} F_2. \tag{3.44}$$

The balance of the latter two terms yields $A_2 = O(\varepsilon^2) \ll A_0 = O(\varepsilon)$; thus (3.34) or (3.40*b*) describes that the Poincaré wave is not effectively excited outside the shock, consistent with the physics. We have thus shown that (3.40) applies to the second scenario, without large k, both inside and outside the shock.

Here, we give a comment on higher-order Poincaré waves. With the same method, we can similarly demonstrate that A_4, which is driven by A_0 and A_2, is governed by

$$A_{4,t} + A_{4,x} + 4 \int A_4 \, \mathrm{d}t = \sqrt{\frac{2}{3}} \left[-\frac{1}{24} A_0^2 - \frac{41}{864} A_2^2 + \frac{17}{72} A_0 A_2 \right]_x. \tag{3.45}$$

The coefficient of $A_0 A_2$, which is $17/72$, is not small, indicating that we do not have a strong reason to consider A_4 as negligible. If we include A_4 to build a three-wave model, we notice that some coefficients in the equation for A_6 are not small either, and this issue persists as we increase the order of the terms. To bolster our A_0–A_2 model, we can make a heuristic argument: in our system, the Kelvin wave A_0 may be more significant because it is the initial wave, the principal driver of the shock and the dominant contributor to the overall energy. Thus, in (3.45), the forcing from A_0^2 might be more crucial, and its small coefficient of $-(1/24)$ may imply that A_4 is not a major component in the wave dynamics. We acknowledge that the formal justification for this assumption is not yet complete, particularly regarding the accuracy of the A_0–A_2 model in predicting the behaviour of shocks driven by strong local nonlinear effects. We will need to rely on numerical simulations to validate our model.

We finally discuss the energy of the system. The total mechanical energy of the equatorial shallow-water system in (2.3), denoted as e, in one period is expressed as

$$e = \frac{1}{2} \int_{-\infty}^{\infty} \int_0^{2\pi/k} \left(u^2 + v^2 + \eta^2 \right) \mathrm{d}x \, \mathrm{d}y. \tag{3.46}$$

By substituting (3.37) into (3.46), we can integrate with respect to y and find that

$$e = \sqrt{\pi} \int_0^{2\pi/k} \left(A_0^2 + \frac{1}{2} A_2^2 \right) \mathrm{d}x. \tag{3.47}$$

It is noted that the contribution from v^2 is again much smaller at large k and can therefore be neglected. Under periodic boundary conditions, it can be shown that if A_0 and A_2 are smooth functions, their governing equations (3.40*a*,*b*) yield $\mathrm{d}e/\mathrm{d}t = 0$, indicating that the energy is conserved. However, when a shock forms, discontinuities in A_0 and A_2 result in energy dissipation. We demonstrate the evolution of energy further in § 4.5.

4. Results and discussion

4.1. *The reduced model*

In § 3, we conducted an asymptotic analysis of the equatorial shallow-water waves with small amplitudes and short wavelengths. We examined the nonlinear evolution following a

https://doi.org/10.1017/jfm.2026.11688 Published online by Cambridge University Press

linear Kelvin wave and derived a reduced model as expressed in (3.40). To obtain a general description of the nonlinear dynamics, we apply the following rescaling:

$$A_0 = \varepsilon K(\theta, \tau), \qquad A_2 = \varepsilon P(\theta, \tau). \tag{4.1}$$

In this context, K and P represent the Kelvin wave and the first Poincaré wave, respectively. The phase θ and modulation time τ were introduced in (3.20), and from (3.36*a*), we set

$$\theta = k(x - t), \qquad \tau = \varepsilon k t. \tag{4.2}$$

We also introduce a parameter γ to quantify the strength of dispersion in relation to nonlinearity, defined as

$$\gamma = \frac{1}{k^2 \varepsilon}, \tag{4.3}$$

upon noticing (3.36*b*). This parameter is also known as the dispersion parameter. Note that the rescalings in (4.2) and (4.3) are chosen to be consistent with the first scenario of large k, where γ is of order unity. In the second scenario, characterised by moderate or small k, the parameter γ becomes large, reflecting the enhanced dispersion inherent to linear Poincaré waves in this regime.

Using (4.1)–(4.3), the evolution (3.40) can be recast to

$$K_\tau = \sqrt{\frac{2}{3}} \left[-\frac{3}{4} K^2 - \frac{3}{16} P^2 + \frac{1}{4} KP \right]_\theta, \tag{4.4a}$$

$$P_\tau - 2\gamma \int P \, \mathrm{d}\theta = \sqrt{\frac{2}{3}} \left[\frac{1}{4} K^2 - \frac{13}{48} P^2 - \frac{3}{4} KP \right]_\theta, \tag{4.4b}$$

with the initial condition specifying that there is a Kelvin wave at early times, expressed as

$$K = \sin\theta, \quad P = 0, \quad \text{as} \quad \tau \to 0. \tag{4.5}$$

The boundary condition is characterised by periodicity in θ with a period of 2π. The integral term in (4.4*b*) is constrained by requiring that its mean over one period vanishes. This constraint guarantees that the integral does not bring in spurious components in addition to waves with phase θ. Once K and P are solved, the quantities u, v and η can be reconstructed by

$$u = \eta = \varepsilon \mathrm{e}^{-y^2/2} \left[K + \left(y^2 - \frac{1}{2} \right) P \right], \quad v = \frac{4\varepsilon}{k} \mathrm{e}^{-y^2/2} y \int P \, \mathrm{d}\theta. \tag{4.6}$$

In the absence of the Poincaré wave, (4.4*a*) simplifies to the Burgers equation for the Kelvin wave, previously derived by Boyd (1980) and Ripa (1982). When $\gamma = 0$, (4.4*a*) and (4.4*b*) reduce to the model proposed by Wang *et al.* (2020) for non-dispersive resonance between the Kelvin wave and the first Poincaré wave. The dispersive term of the Poincaré wave is related to the reduced Ostrovsky equation, also known as the Hunter–Ostrovsky equation, expressed as

$$(u_t + u u_x)_x - u = 0. \tag{4.7}$$

It is a simplified version of the Ostrovsky equation as the Boussinesq dispersion becomes negligibly small (see Ostrovsky (1978), Hunter (1990) and Stepanyants (2020) for details). We can see that the θ-derivative of (4.4*b*), where K is neglected, can be rescaled to (4.7), and indeed, the dispersive term associated with $-u$ arises from rotational effects.

https://doi.org/10.1017/jfm.2026.11688 Published online by Cambridge University Press

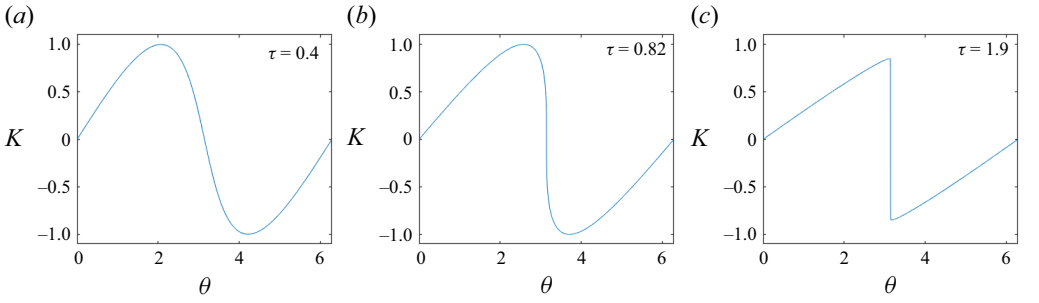


Figure 2. Numerical solutions of (4.8).

Nevertheless, (4.7) is derived from the shallow-water model on an f-plane, and since u is independent of y, it does not accommodate the eigenmode structures in the y direction that we are exploring here, and especially the Kelvin wave is absent in this context. Various aspects of (4.7) have been studied, including periodic waves, solitons (Vakhnenko & Parkes 1998; Stepanyants 2006) and travelling waves, along with their limiting profiles (Boyd 2005*b*). Regarding the shocks with which we are concerned, studies by Hunter (1990), Boyd (2005*a*) and Grimshaw *et al.* (2012) have demonstrated, both numerically and theoretically, that waves with sufficiently short wavelengths or large wave amplitudes tend to develop shocks. Generally, these shocks are much weaker than those found in the Burgers equation. However, this may not hold for our problem, where the non-dispersive Kelvin wave drives the system, as we illustrate in the subsequent analyses.

We solve system (4.4) numerically, using the standard fourth-order Runge–Kutta method for temporal integration and a pseudo-spectral method based on the fast Fourier transform for spatial discretisation. Our results indicate that shocks characterised by discontinuity in the solution will arise despite the presence of dispersion. A typical approach to studying these shocks is to apply the condition of momentum conservation across the discontinuity, which helps determine the shock velocity. Alternatively, we can introduce artificial dissipation to smooth the solution; in the limit of vanishing dissipation, the discontinuous solution is realised. Both approaches yield the same results. In this study, we adopt the second approach. We add $\nu K_{\theta\theta}$ and $\nu P_{\theta\theta}$ to the right-hand side of (4.4*a*) and (4.4*b*), respectively, where ν represents a very small artificial viscosity. The value of ν ranges from 10^{-3} to 10^{-4}, depending on whether the solution converges properly as ν reduces. We demonstrate the numerical solutions for various degrees of dispersion in §§ 4.2–4.4, and subsequently discuss the energy in § 4.5.

4.2. *The non-dispersive cases*

We begin by reviewing the non-dispersive cases, specifically the nonlinear evolution of a Kelvin wave in isolation and the system described by (4.4) with $\gamma = 0$. If we disregard the Poincaré wave P, (4.4*a*) simplifies to an inviscid Burgers equation given by

$$K_\tau + \sqrt{\frac{3}{2}} K K_\theta = 0. \tag{4.8}$$

This equation has been derived by Boyd (1980) and Ripa (1982). Numerical solutions of (4.8) are presented in figure 2. Nonlinearity causes the wave profile to tilt in a clockwise direction, and by $\tau = \sqrt{2/3} \approx 0.82$, a shock forms, characterised by a sudden jump in K across $\theta = \pi$. This shock subsequently develops corners in the wave profile, and the wave amplitude gradually decreases due to energy dissipation at the shock site. Once formed, the

https://doi.org/10.1017/jfm.2026.11688 Published online by Cambridge University Press

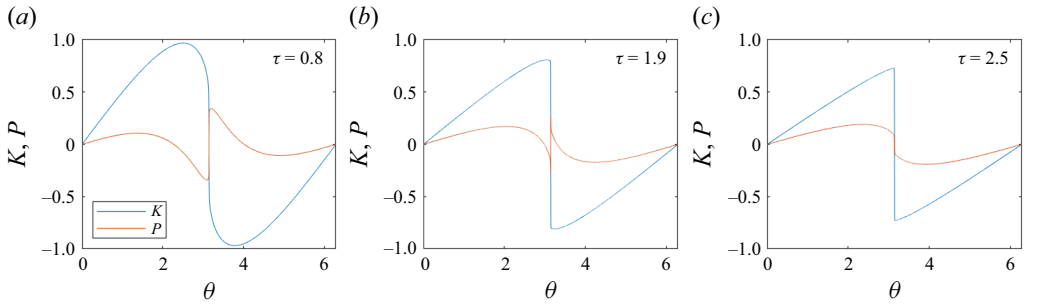


Figure 3. Numerical solutions of system (4.4) with $\gamma = 0$.

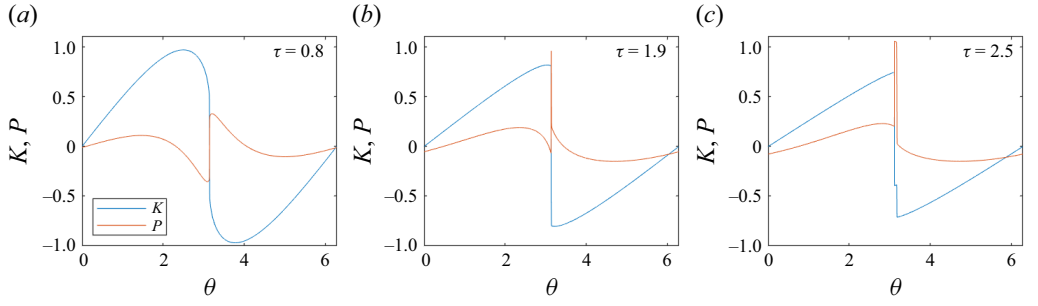


Figure 4. Numerical solutions of system (4.4) with $\gamma = 0.2$.

shock maintains its position at $\theta = \pi$. In the original variables (x, t), the shock propagates at a velocity of unity, which is consistent with the linear Kelvin wave. This can also be demonstrated analytically, as shown by Majda, Rosales & Schonbek (1988) and Carretero-Gonzalez *et al.* (2024). This behaviour is different from the finding of Fedorov & Melville (2000) that the nonlinear Kelvin wave travels faster than its linear counterpart. Their conclusion may stem from their initial condition, which employs a Gaussian profile in the x direction and thus encompasses a range of Fourier modes, in contrast to our initial condition (4.5), which consists of a single Fourier mode.

While the Kelvin wave governed by (4.8) captures the primary dynamics of the shock, the Poincaré wave also reveals important details. System (4.4) with $\gamma = 0$ was analysed by Wang *et al.* (2020), and the results for this scenario are shown in figure 3. The Poincaré wave is triggered by the Kelvin wave and, by $\tau = 0.8$, it also develops a shock. The shock in the Poincaré wave then forms corners, and the jump gradually diminishes. By $\tau = 2.5$, the direction of the jump has reversed. The evolution of the Kelvin wave remains similar to that of a single Kelvin wave as described by (4.8). It is worth noting that Wang *et al.* (2020) only provided insights on the dynamics following figure 3(*c*), where both K and P continue to decay with qualitatively similar profiles. In this context, we present the earlier stage of evolution in figures 3(*a*) and 3(*b*), which will help illustrate the effects of dispersion.

4.3. *The case of weak dispersion*

We now examine the effects of dispersion. We first consider the weak-dispersion regime, where γ is small or moderate, corresponding to our first scenario in the theoretical analysis, in which k is large.

Figure 4 illustrates the evolution of K and P with a small dispersion parameter, $\gamma = 0.2$. At an early time of $\tau = 0.8$, their profiles closely resemble those in the non-dispersive case.

https://doi.org/10.1017/jfm.2026.11688 Published online by Cambridge University Press

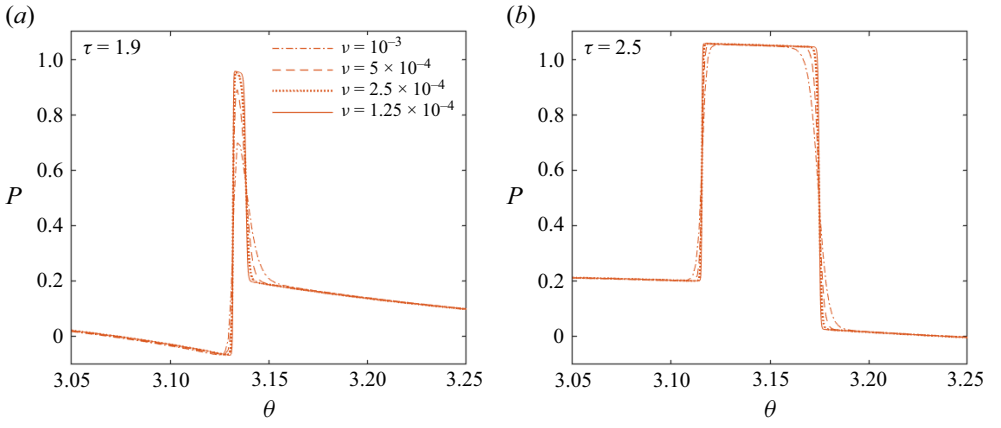


Figure 5. Zoomed-in profiles of the spikes in (*a*) figure 4(*b*) and (*b*) figure 4(*c*) at various artificial viscosities. The solutions with the smallest viscosity, $\nu = 1.25 \times 10^{-4}$, are used for figures 4 and 6.

However, at $\tau = 1.9$, a very sharp spike emerges from one of the corners of the Poincaré wave. This spike has a very small thickness, of the order of 10^{-2}, but its amplitude is significant. It gradually becomes thicker and taller, reaching its peak around $\tau = 2.5$. Additionally, the spike induces a slight twist in the shock of the Kelvin wave. Throughout the evolution, the waves outside the shock behave similarly to the non-dispersive case depicted in figure 3. As time continues, the spike will gradually subside and expand, eventually merging with the outer flow (which is not shown). We do not delve into its late evolution, as wave breaking is likely to occur during its early development.

In figure 5, we zoom in on the spike to reveal its detailed structure. Given that the artificial viscosity ν may influence the small length scale, we gradually reduce ν from 10^{-3} to 1.25×10^{-4} and demonstrate that the profile indeed converges. Our numerical tests also indicate that the limiting profile as $\nu \to 0$ is discontinuous. Although we are using a substantial number of $2^{15} = 32\,768$ Fourier modes for the case of $\nu = 1.25 \times 10^{-4}$, further decreasing ν will lead to the Gibbs phenomenon. Consequently, the spike consists of two shocks that are extremely close to each other, and the dispersion does not regularise the discontinuity.

In figure 6, we present the solutions for η as described in system (4.6), specifically for the cases depicted in figures 4(*b*) and 4(*c*), displayed as contours. We have selected parameters $k = 5$ and $\varepsilon = 0.2$, corresponding to $\gamma = 0.2$. The clearly defined vertical lines at the centre of figures 6(*a*) and 6(*b*) represent the shocks, which are moving eastward at a velocity of unity. The spike of the Poincaré wave contributes to the intricate structures observed in the shock, along with the overshoots extending both southward and northward. It is noted that in some previous studies (e.g. Fedorov & Melville 2000), only the contours downstream of the shock are plotted, likely because the flow upstream of the shock was presumed to be unaffected. However, in our analysis, the flow pattern is nearly antisymmetric around the shock. Additionally, the shock observed in Fedorov & Melville (2000) is considerably convex in the x direction, unlike the vertical straight lines presented here. We suspect this difference arises from their initial condition, which used a Gaussian profile in the x direction, rather than the single Fourier mode considered in our study.

In figure 7, we plot the profiles of η at $y = 0$ and $y = 2$ for the solutions shown in figure 6. The spike of the Poincaré wave results in an overshoot on the shock. The direction of the overshoot is different for $y = 0$ compared with $y = 2$, which is due to the structure of the eigenfunction of the first Poincaré wave (see system (4.6)). It is noted that the

https://doi.org/10.1017/jfm.2026.11688 Published online by Cambridge University Press

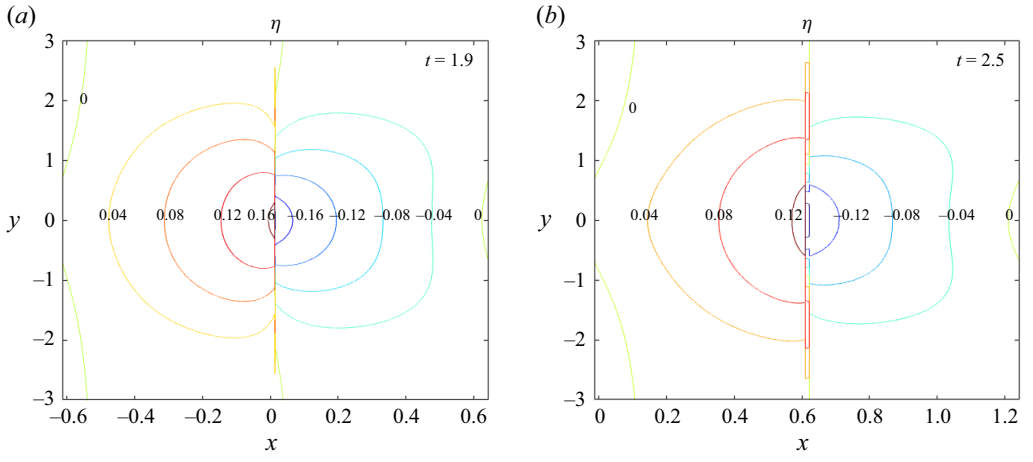


Figure 6. Contour plots of η for (a) figure 4(b) and (b) figure 4(c), obtained with $\varepsilon = 0.2$ and $k = 5$.

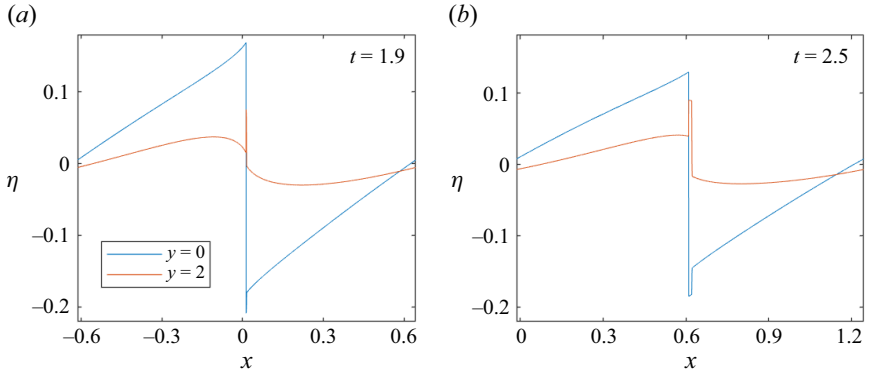


Figure 7. Wave profiles of η at $y = 0$ and $y = 2$ for (a) figure 6(a) and (b) figure 6(b).

Kelvin wave also contributes to the overshoot: the overshoots observed in figure 7 are less pronounced than the spikes shown in figures 4(b) and 4(c). It is found that the twist of K near $\theta = \pi$ (as seen in figure 4c) partially cancels out the spike, thereby weakening the overshoot.

4.4. *The case of strong dispersion*

Strong dispersion occurs for large γ, which aligns with the second scenario where k is not large in our theoretical analysis. In figure 8, we present the numerical solution of system (4.4) at $\gamma = 5$, which is relatively large. At $\tau = 0.8$, the shock from the first Poincaré wave has formed again; however, the profile is quite asymmetric, in contrast to previous cases shown in figures 3(a) and 4(a). It features a downward wedge. The wedge is gradually compressed, and at $\tau = 1.1$, it has evolved into a spike. The spike continues to sharpen, and by $\tau = 1.4$, it reaches an extremely small thickness of approximately 0.015. In this instance, the spike consists of two shocks, similar to those depicted in figures 4(b) and 4(c), but it points in the opposite direction and develops in a significantly different manner. It is worth noting that throughout the evolution, the shock travels at a constant speed (as evidenced by its remaining stationary at $\theta = \pi$), and the first Poincaré wave is prominently excited only within the narrow shock region. These observations are consistent with the

https://doi.org/10.1017/jfm.2026.11688 Published online by Cambridge University Press

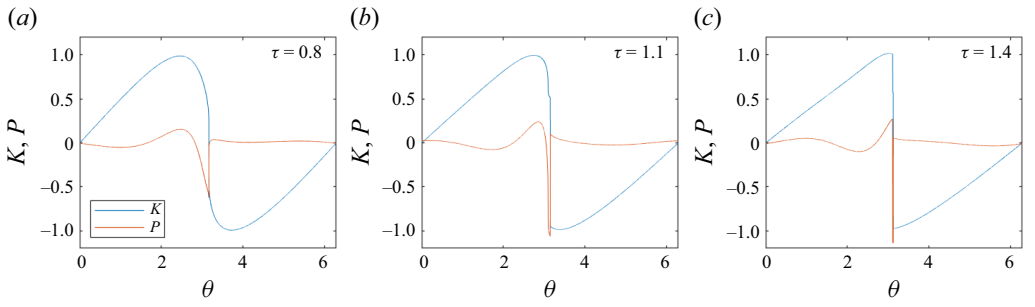


Figure 8. Numerical solution of system (4.4) obtained with $\gamma = 5$.

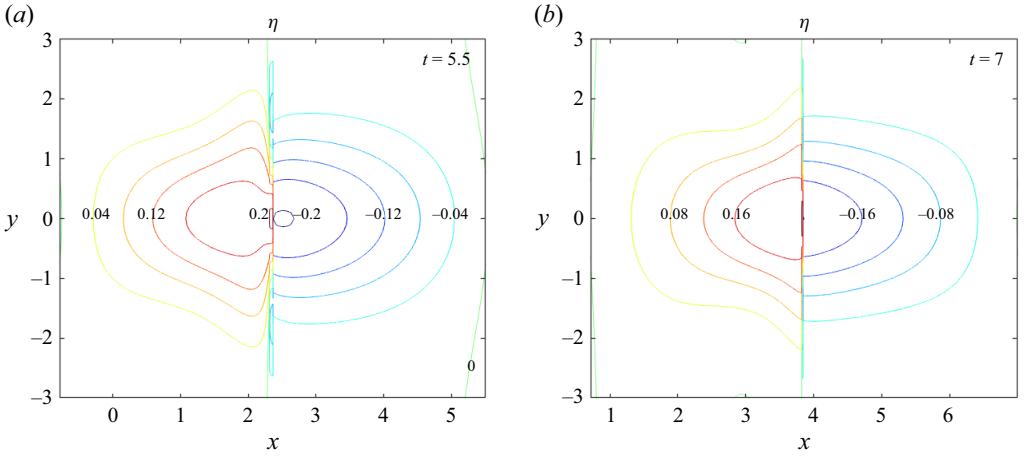


Figure 9. Contour plots of η for the solution of figure 8(b,c), obtained with $\varepsilon = 0.2$ and $k = 1$.

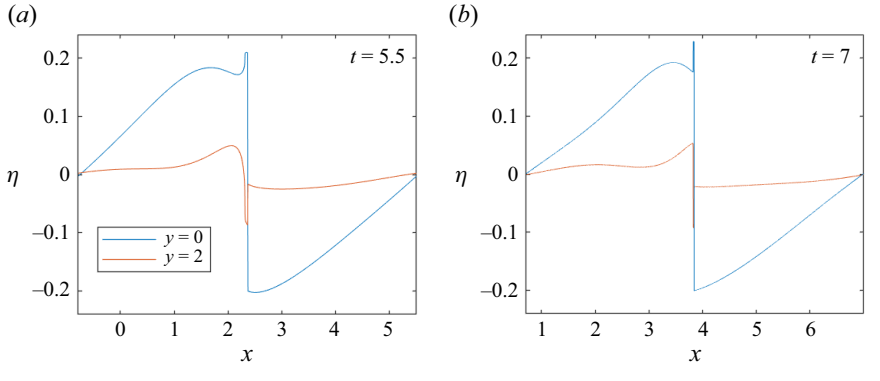


Figure 10. Wave profiles of η for figure 9 at $y = 0$ and $y = 2$.

fundamental assumptions and expectations outlined in the theoretical analysis (refer to the discussion around (3.42)).

To demonstrate the solution of η, we set $\varepsilon = 0.2$ and $k = 1$ (which corresponds to $\gamma = 5$). The results are plotted in figures 9 and 10. The contours in figure 9 reveal a shock at the centre accompanied by small-scale structures, while the profiles in figure 10 feature overshoots that gradually increase in strength. Compared with figures 6 and 7, the

https://doi.org/10.1017/jfm.2026.11688 Published online by Cambridge University Press

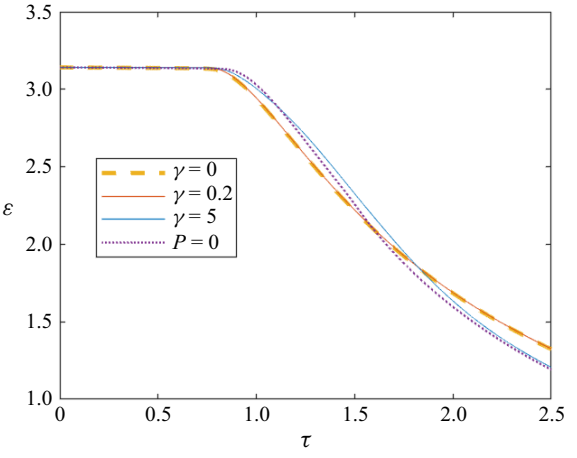


Figure 11. Evolution of energy described by (4.9) for various values of γ. The curve $P = 0$ corresponds to the case of the pure Kelvin wave modelled by (4.8).

contours are more asymmetric, the shocks appear more distorted and the overshoots point in opposite directions.

We observe spike formations for both strong and weak dispersion, although they exhibit different behaviours. Our findings indicate that these formations occur for any $\gamma > 0$, placing them in either of the two categories, suggesting that spike formation is quite generic. Additionally, we note that this phenomenon has not been documented in previous studies of dispersive shock waves. In the KdV equation or the NLS equation, dispersion regularises the discontinuity of the shock, resulting in a large number of high-frequency quasi-periodic oscillations (El & Hoefer 2016). In contrast, the reduced Ostrovsky equation features shocks with discontinuities that are similar to, but much weaker than, those found in the Burgers equation (Hunter 1990; Boyd 2005*a*; Grimshaw *et al.* 2012). The spike, consisting of two shocks very close together, appears to form a more complex structure.

4.5. *Energy*

We briefly discuss the energy of the system. Using the rescaled variables defined in § 4.1, the energy of (3.47) can be expressed as

$$e = \sqrt{\pi}\frac{\varepsilon^2}{k}\mathcal{E}, \qquad \mathcal{E}(\tau) = \int_0^{2\pi} \left(K^2 + \frac{1}{2}P^2\right) \mathrm{d}\theta. \tag{4.9}$$

In figure 11, we plot the evolution of $\mathcal{E}$ for the three values of γ that we have considered. We also include the case of a pure Kelvin wave described by (4.8), which is denoted as $P = 0$ in the legend. The energy $\mathcal{E}$ remains constant before $\tau \approx 0.8$, confirming energy conservation for smooth wave profiles. After that point, $\mathcal{E}$ begins to decay due to dissipation caused by shocks. The energy for $\gamma = 0.2$ is nearly the same as that for $\gamma = 0$, since the wave profiles in these two cases are almost identical, except for the spike of the Poincaré wave (see figures 3 and 4), which has a negligible effect on the integral in θ. Overall, the decay behaviours are similar across cases, indicating that energy is primarily dissipated by the Kelvin wave shock. The influence of the Poincaré wave and its associated dispersion on the system's energy is relatively weak.

https://doi.org/10.1017/jfm.2026.11688 Published online by Cambridge University Press

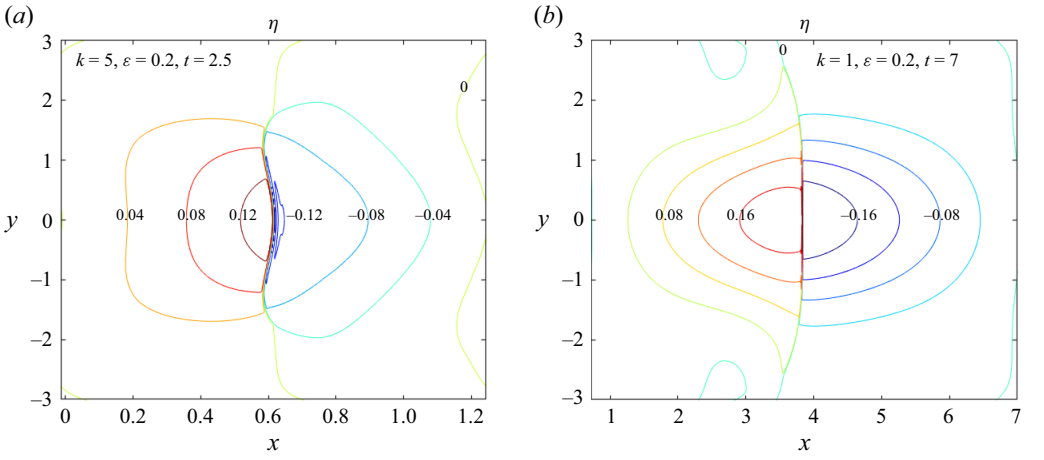


Figure 12. Contour plots of η obtained from numerical simulations corresponding to (*a*) figure 6(*b*) and (*b*) figure 9(*b*).

5. Numerical simulation

To confirm our theoretical findings, we conduct direct numerical simulations using the equatorial shallow-water model. We solve system (2.3) with the initial condition of a Kelvin wave:

$$u = \eta = \varepsilon \sin(kx)\mathrm{e}^{-y^2/2}, \quad v = 0 \qquad \text{at } t = 0. \tag{5.1}$$

We consider $\varepsilon = 0.2$ and compare the wavenumbers $k = 5$ and $k = 1$, as examined in §§ 4.3 and 4.4. Since the evanescent boundary condition at $y \to \pm\infty$ is not feasible for numerical simulations, we replace it by setting $u = v = h = 0$ at $y = \pm\pi$. This adjustment provides a reasonable approximation, as wave amplitudes decay rapidly, following the trend of $\mathrm{e}^{-(y^2/2)}$.

We use a finite-volume method for spatial discretisation within a square domain defined by $[-\pi, \pi] \times [-\pi, \pi]$. This domain is discretised using a uniform Cartesian mesh of size 2000×2000. To approximate the variables at the interface of grids, we employ a Roe-type local mean and utilise a local Lax–Friedrichs splitting scheme to evaluate the Riemann flux (Toro 2013). Next, we apply a fifth-order weighted essentially non-oscillatory (WENO) reconstruction using a five-point stencil to obtain one-sided face states. The smoothness indicators and nonlinear weights follow the approach outlined by Borges *et al.* (2008). Small amounts of artificial dissipation have been added in the vicinity of the shocks to remove spurious oscillations.

Time marching is achieved using a strong-stability-preserving Runge–Kutta (SSPRK) scheme, specifically employing the classical third-order total variation diminishing Runge–Kutta developed by Shu & Osher (1988). The time step is dynamically constrained by a dimensionally split Courant–Friedrichs–Lewy condition, which is based on the maximum local signal speed and the stability criterion of the WENO–Rusanov–SSPRK combination (Gottlieb, Shu & Tadmor 2001; LeVeque 2002).

We focus on the cases shown in figures 6(*b*) and 9(*b*) for our numerical simulations, with the corresponding results for η displayed in figures 12(*a*) and 12(*b*). The numerical simulations predict wave patterns and shock formation that closely match theoretical expectations. Notably, the shock depicted in figure 12(*a*) has a thicker structure compared with that in figure 12(*b*), which correlates with the observations made in figures 6(*b*) and

https://doi.org/10.1017/jfm.2026.11688 Published online by Cambridge University Press

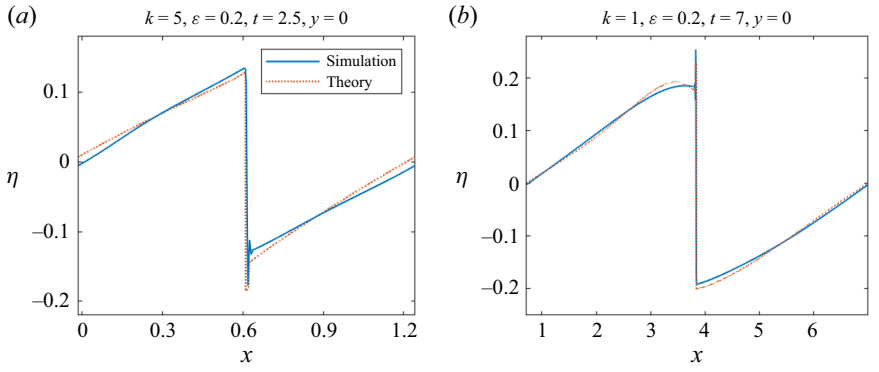


Figure 13. Comparisons of η at $y = 0$ between numerical results (blue solid lines) and theoretical predictions (red dashed lines).

9(*b*). However, there are some differences in the detailed structure of the shock between the simulations and the theory, particularly when comparing figures 6(*b*) and 12(*a*). These discrepancies are primarily due to the limited resolution of the numerical simulations at the shocks. Additionally, higher-order terms neglected in the theoretical analysis may contribute to these differences. Furthermore, the boundary truncated at $y = \pm\pi$ might have affected the shocks as $|y|$ increases. Despite these issues, there is overall qualitative agreement between the theory and the simulations.

In figure 13, we compare the profiles of η at $y = 0$ from the numerical simulation with the theoretical results previously shown in figures 7(*b*) and 10(*b*). The wave profiles show good quantitative agreement. In particular, the numerical solutions exhibit overshoots at the shocks and qualitatively resemble the theoretical predictions. There are subtle differences in the detailed structure of the overshoot, which may be attributed to the limitations of both the theoretical analysis and the numerical simulation. In our theoretical analysis, we neglected higher-order Poincaré waves, which could lead to more complex overshoot structures. On the other hand, numerical simulations may suffer from insufficient resolution, as it is impractical to use a very large number of Fourier modes to fully resolve the small scale of the shock. Nonetheless, it is clear that the numerical simulation reproduces the overshoot predicted by the theory with qualitative agreement. Therefore, we can conclude that the reduced model effectively captures the main dynamics of the nonlinear waves.

6. Conclusions and remarks

In this paper, we have studied dispersive shocks in equatorial shallow-water waves. Previous research indicates that a Kelvin wave evolves into a shock due to its non-dispersive nature. In our study, we demonstrate that a Kelvin wave can excite the first Poincaré wave, which is inherently dispersive, and we have shown how this dispersion influences the dynamics of the shock.

We conducted a theoretical analysis of the nonlinear evolution of the Kelvin wave and the first Poincaré wave. From this, we derived a reduced model in which the effects of dispersion are represented by an integral term, resembling the rotational term of the Ostrovsky equation. Numerical solutions of the reduced model indicate that dispersion leads to a sharp spike in the Poincaré wave, causing an overshoot in the shock. This spike consists of two shocks that are positioned extremely close to each other. The spike emerges in both strong and weak dispersion, but it forms and evolves in very different ways in each

https://doi.org/10.1017/jfm.2026.11688 Published online by Cambridge University Press

case. The spike has a minor impact on wave energy, as most energy is dissipated through the shock of the Kelvin wave. To validate our theory, we performed numerical simulations based on the primitive equatorial shallow-water equations.

For prospective research, our current model serves as an idealised framework featuring a single Kelvin wave in the initial condition. However, it would be beneficial to explore other initial conditions. For instance, an initial Poincaré wave with a large wavenumber could also stimulate a Kelvin wave, but the nonlinear dynamics might differ. Additionally, the nonlinear evolution of an initial Gaussian profile, as examined by Fedorov & Melville (2000), is of great interest. The resulting shock exhibits a convex profile, and the detailed dynamics surrounding it raises intriguing yet challenging questions. The present analysis can be extended to incorporate additional dispersive mechanisms, such as KdV-type dispersion, which similarly facilitates nonlinear interactions between Kelvin and Poincaré waves (Tomasson & Melville 1990). The interplay between KdV dispersion and Poincaré-wave dispersion represents an intriguing avenue for future research.

The spike formation within the dispersive shock is a novel phenomenon and also raises new questions. Our simplified model suggests that the interaction between dispersion and the shock is responsible for the emergence of the spike. However, the exact mechanism behind its formation remains unclear. Furthermore, numerical simulations indicate that the spike may have a more complex structure than our model predicts. Understanding the detailed structure of the spike poses a significant challenge for both theoretical analysis and numerical simulation.

The implications of the spike and the overshoot in the ocean and the atmosphere are also worth exploring. It may suggest a violent wave breaking and a more distorted thermocline in the ocean. As for the atmosphere, we have not incorporated the crucial factor of moisture convection in our model, as it presents a significant theoretical challenge. Nonetheless, our findings may offer valuable insights into these more complex issues. The simulations conducted by Rostami & Zeitlin (2020) and Cao *et al.* (2025) indicate that moisture can slow down Kelvin waves and lead to interactions with the modon. Notably, Cao *et al.* (2025) identified Poincaré waves that exhibit much finer structures than both the modon and the Kelvin wave, as shown in their figure 10. The small-scale spikes observed in our study could help explain these phenomena.

Acknowledgements. The authors would like to thank Dr H. Hajduk (TU Dortmund University) for insightful discussions on this topic and Dr X. Luo (Academy of Mathematics and Systems Science, CAS) for providing literature on dispersive shock waves. We also thank the referees for their constructive comments and for providing us with important literature on the Ostrovsky equation and on the MJO understood as modons.

Funding. C.W. acknowledges the start-up funds for young scholars offered by Beijing Normal University (no. 312200502507) and Beijing Normal–Hong Kong Baptist University (no. UICR0700081-24). D.S. was supported by the National Natural Science Foundation of China (nos. 52201325, W2421012). Z.W. was supported by the National Science Foundation of China (nos. 12325207, 42450111, 12132018).

Declaration of interests. The authors report no conflict of interest.

Appendix A. The excitation of the first Poincaré wave

In this appendix, we demonstrate details on the excitation of the first Poincaré wave by a linear Kelvin wave. We limit our attention to the first scenario, in which k is large, where linear Poincaré and Kelvin waves have nearly identical phase velocities. We demonstrate the excitation through a weakly nonlinear analysis based on a regular perturbation expansion in terms of the order of the wave amplitude ε:

$$(u, v, \eta) = \varepsilon \left(u^L, v^L, \eta^L\right) + \varepsilon^2 \left(u', v', \eta'\right) + o\left(\varepsilon^2\right). \tag{A1}$$

https://doi.org/10.1017/jfm.2026.11688 Published online by Cambridge University Press

The variables with superscript L are the linear waves discussed in § 3.1, and the prime denotes the nonlinear components. In this context, the nonlinear waves are of $O(\varepsilon)$ weaker than the linear waves and are driven by the latter. We again introduce the variables to proceed with the analysis:

$$S' = \eta' + u', \quad D' = \eta' - u'. \tag{A2}$$

By substituting (A1) into the system described by (2.3) and collecting the terms of order $O(\varepsilon^2)$, we can manipulate the resulting equations to obtain

$$S'_t + S'_x + \left(\frac{\partial}{\partial y} - y\right) v' = -u^L u^L_x - \left(u^L \eta^L\right)_x - v^L u^L_y - \left(v^L \eta^L\right)_y \equiv F^L, \tag{A3a}$$

$$v'_t + \frac{1}{2}\left(\frac{\partial}{\partial y} + y\right) S' + \frac{1}{2}\left(\frac{\partial}{\partial y} - y\right) D' = -u^L v^L_x - v^L v^L_y \equiv E^L, \tag{A3b}$$

$$D'_t - D'_x + \left(\frac{\partial}{\partial y} + y\right) v'_x = u^L u^L_x - \left(u^L \eta^L\right)_x + v^L u^L_y - \left(v^L \eta^L\right)_y \equiv G^L. \tag{A3c}$$

The weakly nonlinear waves have the same differential operator as the linear system (3.3), and are driven by the non-homogeneous terms composed of the linear waves. We again perform an eigenfunction expansion:

$$\begin{aligned}\left(S', v', D', F^L, E^L, G^L\right) &= \mathrm{e}^{-y^2/2} \\ &\times \sum_{n=0}^{\infty} \left[S'_n(x,t), v'_n(x,t), D'_n(x,t), F^L_n(x,t), E^L_n(x,t), G^L_n(x,t)\right] \frac{H_n(y)}{2^n},\end{aligned} \tag{A4}$$

and determine the equations for each order:

$$S'_{0,t} + S'_{0,x} = F^L_0, \tag{A5}$$

$$S'_{1,t} + S'_{1,x} - v_0 = F^L_1, \quad v'_{0,t} + S'_1 = E^L_0, \tag{A6}$$

$$S'_{n,t} + S'_{n,x} - v'_{n-1} = F^L_n, \tag{A7a}$$

$$v'_{n-1,t} + nS'_n - \frac{1}{2} D'_{n-2} = E^L_{n-1}, \tag{A7b}$$

$$D'_{n-2,t} - D'_{n-2,x} + 2(n-1) v'_{n-1} = G^L_{n-2}, \quad n \geq 2. \tag{A7c}$$

Term F^L_n is calculated by projecting F^L onto the eigenspace of H_n:

$$F^L_n = \frac{\displaystyle\int_{-\infty}^{\infty} F^L H_n(y) \mathrm{e}^{-y^2/2}\, \mathrm{d}y}{\sqrt{\pi} n!}, \tag{A8}$$

and similar expressions for E^L_n and G^L_n. In the large-k limit, one can show that weakly nonlinear waves feature similar properties to linear waves shown in (3.13)–(3.17):

$$v'_{n-1} = -n \int S'_n \, \mathrm{d}t, \qquad u'_n = \eta'_n = \frac{S'_n}{2} \equiv A'_n, \tag{A9}$$

and D'_n is again significantly smaller. The equation of A'_n then follows from (A7a):

$$A'_{n,t} + A'_{n,x} + n \int A'_n \, \mathrm{d}t = \frac{1}{2} F^L_n. \tag{A10}$$

https://doi.org/10.1017/jfm.2026.11688 Published online by Cambridge University Press

Note that the contributions of E^L_{n-1} and G^L_{n-2} to (A9) and (A10) are $o(k^{-1})$ smaller. The initial condition for (A10) is $A'_n = 0$ at $t = 0$, and the boundary condition requires that A'_n has the same periodicity as F^L_n. To compute F^L_n, recall that we consider the evolution following a linear Kelvin wave (cf. (3.22)). Thus,

$$u^L = \eta^L = \mathrm{e}^{-y^2/2}\sin(kx - kt), \quad v^L = 0. \tag{A11}$$

The resulting F^L, according to (A3*a*), is

$$F^L = -\frac{3}{2}\mathrm{e}^{-y^2}\left[\sin^2(kx - kt)\right]_x. \tag{A12}$$

Computing the projection according to (A8), we find that F_n is zero for odd n, because F^L is even in y but $H_n(y)$ is odd for odd n (see (3.5)). Specifically, $F^L_1 = 0$ indicates that Kelvin waves do not excite Yanai waves. For even n, we can calculate the projection to find

$$\begin{aligned} F^L_0 &= \sqrt{\frac{2}{3}}\left[-\frac{3}{2}\sin^2(kx - kt)\right]_x, \quad F^L_2 = \sqrt{\frac{2}{3}}\left[\frac{1}{2}\sin^2(kx - kt)\right]_x, \\ F^L_4 &= \sqrt{\frac{2}{3}}\left[\frac{1}{12}\sin^2(kx - kt)\right]_x, \quad F^L_6 = \sqrt{\frac{2}{3}}\left[\frac{1}{108}\sin^2(kx - kt)\right]_x, \quad \ldots. \end{aligned} \tag{A13}$$

The projection significantly weakens starting from $n = 4$, so the system of $n = 0$ and $n = 2$, corresponding to the newly excited Kelvin wave and first Poincaré wave, may account for the dominant dynamics. Substituting F^L_0 and F^L_2 into (A10), we can solve that

$$\begin{aligned} A'_0 &= -\frac{1}{2}\sqrt{\frac{3}{2}}\,kt\sin(2kx - 2kt), \\ A'_2 &= -\frac{1}{4}\sqrt{\frac{2}{3}}\,k^2\left[\cos(2kx - 2kt) - \cos\left(2kx - 2kt - \frac{t}{k}\right)\right]. \end{aligned} \tag{A14a,b}$$

Equation (A14*a*) demonstrates an algebraic growth of the newly excited Kelvin wave, which results from resonance with the fundamental linear Kelvin wave. Over a sufficiently long time, A'_0 will grow to a substantial amplitude. The first Poincaré wave A'_2 described by (A14*b*) behaves differently under weak dispersion. Wave A'_2 also exhibits algebraic growth at early times when t/k is small, but at later times, A_2 saturates at large amplitudes of $O(k^2)$. When A'_0 and A'_2 reach the amplitude of $O(\varepsilon^{-1})$, the regular perturbation expansion (A1) becomes disorganised, signalling the waves' transition into the next stage of nonlinear evolution, which we have studied in § 3.2. This happens when

$$A'_0 = O(kt) \sim \varepsilon^{-1}, \quad A'_2 = O\left(k^2\right) \sim \varepsilon^{-1}, \tag{A15}$$

which means $k \sim t \sim \varepsilon^{-(1/2)}$, consistent with the scale for nonlinear evolution shown in (3.36). Notably, S_2 that appears in (3.27*a*) corresponds to

$$S_2 = \varepsilon^2\left(2A'_2\right) = O(\varepsilon), \tag{A16}$$

and, therefore, we have shown that the first Poincaré wave can be excited to reach the same order as the Kelvin wave shown in (3.29).

References

BENNETT, J.R. 1973 A theory of large-amplitude Kelvin waves. *J. Phys. Oceanogr.* **3**, 57–60.

BORGES, R., CARMONA, M., COSTA, B. & DON, W.S. 2008 An improved weighted essentially non-oscillatory scheme: WENO-Z. *J. Comput. Phys.* **227**, 3191–3211.

https://doi.org/10.1017/jfm.2026.11688 Published online by Cambridge University Press

BOUCHUT, F., LE SOMMER, J. & ZEITLIN, V. 2005 Breaking of balanced and unbalanced equatorial waves. *Chaos* **15**, 013503.
BOYD, J.P. 1980 The nonlinear equatorial Kelvin wave. *J. Phys. Oceanogr.* **10** (1), 1–11.
BOYD, J.P. 1983 Long wave/short wave resonance in equatorial waves. *J. Phys. Oceanogr.* **13** (3), 450–458.
BOYD, J.P. 2005*a* Microbreaking and polycnoidal waves in the Ostrovsky–Hunter equation. *Phys. Lett. A* **338**, 36–43.
BOYD, J.P. 2005*b* Ostrovsky and Hunter's generic wave equation for weakly dispersive waves: matched asymptotic and pseudospectral study of the paraboloidal travelling waves (corner and near-corner waves). *Euro. J. Appl. Maths* **16** (6), 65–81.
BURGERS, J.M. 1948 A mathematical model illustrating the theory of turbulence. *Adv. Math.* **1**, 171–199.
CAO, Y., KURGANOV, A., LIU, Y., ROSTAMI, M. & ZEITLIN, V. 2025 On the dynamics of equatorial excited dipolar systems. *Phys. Fluids* **37**, 056618.
CARRETERO-GONZALEZ, R., FRANTZESKAKIS, D.J. & KEVREKIDIS, P.G. 2024 *Nonlinear Waves & Hamiltonian Systems*. Oxford University Press.
EL, G.A. & HOEFER, M.A. 2016 Dispersive shock waves and modulation theory. *Physica D* **333**, 11–65.
FEDOROV, A.V. & BROWN, J.N. 2009 *Equatorial Waves*. Elsevier Ltd.
FEDOROV, A.V. & MELVILLE, W.K. 1995 Propatation and breaking of nonlinear Kelvin waves. *J. Phys. Oceanogr.* **25**, 2518–2531.
FEDOROV, A.V. & MELVILLE, W.K. 2000 Kelvin fronts on the equatorial thermocline. *J. Phys. Oceanogr.* **30**, 1692–1705.
GOTTLIEB, S., SHU, C.-W. & TADMOR, E. 2001 Strong stability-preserving high-order time discretization methods. *SIAM Rev.* **43**, 89–112.
GRIMSHAW, R.H.J., HELFRICH, K. & JOHNSON, E.R. 2012 The reduced Ostrovsky equation: integrability and breaking. *Stud. Appl. Maths* **129** (4), 414–436.
HUNTER, J.K. 1990 Numerical solution of some nonlinear dispersive wave equations. *Lectures Appl. Maths* **26**, 301–316.
KILADIS, G.N., WHEELER, M.C., HAERTEL, P.T., STRAUB, K.H. & ROUNDY, P.E. 2009 Convectively coupled equatorial waves. *Rev. Geophys.* **47** (2), 2008RG000266.
LE SOMMER, J., REZNIK, G.M. & ZEITLIN, V. 2004 Nonlinear geostrophic adjustment of long-wave disturbances in the shallow-water model on the equatorial beta-plane. *J. Fluid Mech.* **515**, 135–170.
LEVEQUE, R.J. 2002 *Finite Volume Methods for Hyperbolic Problems*. Cambridge University Press.
LIGHTHILL, J. 1978 *Waves in Fluids*. Cambridge University Press.
MAJDA, A., ROSALES, R. & SCHONBEK, M. 1988 A canonical system of integrodifferential equations arising in resonant nonlinear acoustics. *Stud. Appl. Maths* **79**, 205–262.
MAJDA, A.J., ROSALES, R.R., TABAK, E.G. & TURNER, C.V. 1999 Interaction of large-scale equatorial waves and dispersion of Kelvin waves through topographic resonances. *J. Atmos. Sci.* **56** (24), 4118–4133.
MATSUNO, T. 1966 Quasi-geostrophic motions in the equatorial area. *J. Met. Soc. Japan* **44** (1), 25–43.
OSTROVSKY, L.A. 1978 Nonlinear internal waves in a rotating ocean. *Oceanology* **18**, 119–125.
PEDLOSKY, J. 2013 *Geophysical Fluid Dynamics*. Springer Science & Business Media.
RIPA, P. 1982 Nonlinear wave–wave interactions in a one-layer reduced-gravity model on the equatorial β plane. *J. Phys. Oceanogr.* **12** (1), 97–111.
RIPA, P. 1983*a* Weak interactions of equatorial waves in a one-layer model. Part I: general properties. *J. Phys. Oceanogr.* **13** (7), 1208–1226.
RIPA, P. 1983b Weak interactions of equatorial waves in a one-layer model. Part II: applications. *J. Phys. Oceanogr.* **13** (7), 1227–1240.
ROSTAMI, M. & ZEITLIN, V. 2019*a* Eastward-moving convection-enhanced modons in shallow water in the equatorial tangent plane. *Phys. Fluids* **31**, 021701.
ROSTAMI, M. & ZEITLIN, V. 2019*b* Geostrophic adjustment on the equatorial beta-plane revisited. *Phys. Fluids* **31**, 021701.
ROSTAMI, M. & ZEITLIN, V. 2020 Can geostrophic adjustment of baroclinic disturbances in the tropical atmosphere explain MJO events? *Q. J. R. Meteorol. Soc.* **146**, 3998–4012.
ROSTAMI, M., ZHAO, B. & PETRI, S. 2022 On the genesis and dynamics of Madden–Julian oscillation-like structure formed by equatorial adjustment of localized heating. *Q. J. R. Meteorol. Soc.* **148**, 3788–3813.
SHU, C.-W. & OSHER, S. 1988 Efficient implementation of essentially non-oscillatory shock-capturing schemes, II. *J. Comput. Phys.* **83**, 32–78.
STEPANYANTS, Y.A. 2006 On stationary solutions of the reduced Ostrovsky equation: periodic waves, compactons and compound solitons. *Chaos Solitons Fractals* **28**, 194–204.
STEPANYANTS, Y.A. 2020 Nonlinear waves in a rotating ocean (the Ostrovsky equation and its generalizations and applications). *Izv. Atmos. Ocean. Phys.* **56** (1), 16–32.

https://doi.org/10.1017/jfm.2026.11688 Published online by Cambridge University Press

STRAUB, K.H., KILADIS, G.N. & CIESIELSKI, P.E. 2006 The role of equatorial waves in the onset of the South China Sea summer monsoon and the demise of El Niño during 1998. *Dyn. Atmos Oceans* **42** (1–4), 216–238.

TOMASSON, G.G. & MELVILLE, W.K. 1990 Nonlinear and dispersive effects in Kelvin waves. *Phys. Fluids* **37**, 189–193.

TORO, E.F. 2013 *Riemann Solvers and Numerical Methods for Fluid Dynamics: a Practical Introduction*. Springer.

VAKHNENKO, V.O. & PARKES, E.J. 1998 The two loop soliton solution of the Vakhnenko equation. *Nonlinearity* **11** (6), 1457–1464.

WALLACE, J.M. & KOUSKY, V.E. 1968 Observational evidence of Kelvin waves in the tropical stratosphere. *J. Atmos. Sci.* **25** (5), 900–907.

WANG, M., WANG, Z. & HAJDUK, H. 2020 Nonlinear interactions of nearly non-dispersive equatorial shallow-water waves. *IMA J. Appl. Maths* **85** (3), 365–384.

WHITHAM, G.B. 1974 *Linear and Nonlinear Waves*. Wiley.

YANAI, M. & MARUYAMA, T. 1966 Stratospheric wave disturbances propagating over the equatorial pacific. *J. Met. Soc. Japan II* **44** (5), 291–294.

YANO, J.-I. & TRIBIA, J.J. 2017 Tropical atmosphere Madden–Julian oscilations: a strongly nonlinear free solitary Rossby wave? *J. Atmos. Sci.* **74**, 3473–3489.

https://doi.org/10.1017/jfm.2026.11688 Published online by Cambridge University Press